Nanoscale

Accepted Manuscript

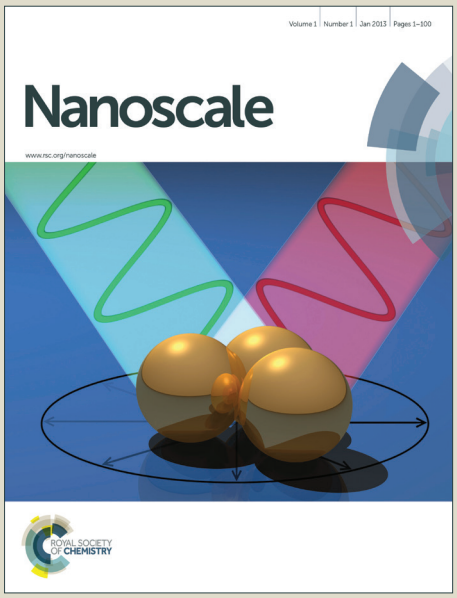

Cite this: DOI: 10.1039/c0xx00000x

www.rsc.org/xxxxxx

ARTICLE TYPE

Fabrication of MoS_2 nanosheets@TiO_2 nanotubes hybrid nanostructures for lithium storage

Xin Xu,[a] Zhaoyang Fan,[a] Shujiang Ding,[a]* Demei Yu[a]* and Yaping Du[b]

[a] *State Key Laboratory for Mechanical Behavior of Materials and MOE Key Laboratory for Nonequilibrium Synthesis and Modulation of Condensed Matter and Department of Applied Chemistry, School of Science, Xi'an Jiaotong University, Xi'an 710049, China.*
[b] *Frontier Institute of Chemistry, Frontier Institute of Science and Technology jointly with College of Science, Xi'an Jiaotong University, Xi'an 710054, China.*

Received (in XXX, XXX) Xth XXXXXXXXX 20XX, Accepted Xth XXXXXXXX X 20XX
DOI: 10.1039/b000000x

MoS_2 nanosheets@TiO_2 nanotubes hybrid nanostructures were successfully prepared by a facile two-step method: prefabricate porous TiO_2 nanotubes based on a sol–gel method template again polymeric nanotubes, and then assemble MoS_2 nanoclusters that consist of ultrathin nanosheets through a solvothermal process. These hybrid nanostructures were characterized by scanning electron microscopy (SEM), transmission electron microscopy (TEM), energy dispersive X-ray (EDX) spectroscopy, X-ray diffraction (XRD) and Brunauer–Emmett–Teller (BET) analyzer. When evaluated as an electrode material for lithium ion batteries, the results of electrochemical test show that the unique MoS_2 nanosheets@TiO_2 nanotubes hybrid nanostructures exhibits outstanding lithium storage performances with high specific capacity and excellent rate capability. The smart architecture of the MoS_2 nanosheets@TiO_2 nanotubes hybrid nanostructures makes a prominent contribution to the excellent electrochemical performance.

1. Introduction

Rechargeable lithium ion batteries (LIBs) are considered as one of the most promising energy storage devices and a priority candidate for all electrical vehicles, which is crucial for the reduction of pollutant gaseous emissions arising from transportation.[1] Although widely used as anode materials in commercial Li-ion batteries (LIBs), graphite has a relatively low theoretical capacity (372 mA h g^{-1}) and cannot meet the need of large-scale batteries in the future.[2,3] In recent years, transition metal oxides and sulfides have been widely investigated as the active materials for lithium storage based on their relatively high energy density, long cycle life, design flexibility and environmental friendliness.[4-7] Nevertheless, the charge/discharge process in current lithium ion batteries at a high current rate can cause a high level of polarization for bulk electrode materials and degrade the electrochemical properties of the batteries.[8] In addition, the electrode materials' large volume change accompanying the process of Li^+ ion charge–discharge (alloying/de-alloying) and the cyclic stress break down the conductive path between the active material and black carbon give rise to the fast fading in capacity upon extended cycling. To solve the problem above, one feasible strategy is to design and prepare hollow, hierarchical and porous nanostructures. During the charge/discharge process of lithium ion batteries, the space exists in these electrode nanomaterials can store more lithium ions, buffer the large volume change to some extent, decrease lithium ions' and electrolyte diffusion length simultaneously, thus leading to improvement in cycling capacity retention upon extended cycling. [9]

Molybdenum disulfide (MoS_2), a typical layered inorganic material, has received great interest as a kind of promising electrode material for LIBs in recent years.[10-13] Thus far, many nanostructures of MoS_2 such as nanoflakes, nanotubes and nanoflowers have been reported for lithium storage.[14-16] Although these MoS_2 nanostructures exhibit high capacities up to 1000 mA h g^{-1}, the inferior cycling stability impedes their practical application as electrode materials of LIBs. Titanium dioxide (TiO_2), which possesses a low Li-ion diffusivity and electronic conductivity, reveals a relatively low discharge capacity. However, due to the low volume variation (<4%) during the charge–discharge process,[17-19] TiO_2 based electrode materials generally display favorable cyclical stability compared to other transition metal oxides and sulfides based nanomaterials.[20,21] To overcome the inherent defects of the MoS_2 and TiO_2 based electrode

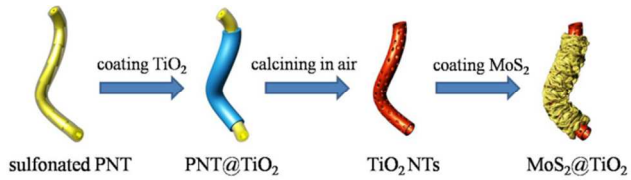

Scheme 1 Schematic illustration of the synthetic procedure of MoS_2 nanosheets@TiO_2 nanotubes hybrid nanostructures.

materials, one doable strategy is to design smart hybridization of them. By combining the individual constituents, some new properties which are difficult to achieve in a single system were presented, such as a high capability to absorb the volume variation of the active material during lithium insertion and the ability to react reversibly with a larger amount of lithium.[22-24] On the basis of this guesswork, a great deal of hybrid nanostructures have already been fabricated for lithium ion batteries such as SnO_2-TiO_2,[19,25,26] NiO-ZnO,[27,28] SnO_2–NiO,[29] Fe_2O_3-NiO[30] and TiO_2-Fe_2O_3.[31] To build up an integrated smart architecture, an inactive or less active composition is usually used as a supporting or conducting matrix to buffer the volume change or facilitate the reactions.[16,21] Accordingly, to design the hybridization TiO_2–MoS_2 system, the stable TiO_2 should be used as the skeleton of the hybrid system, and the MoS_2 with high capacity can be loaded on the skeleton. To the best of our knowledge, a number of TiO_2–MoS_2 composites have been investigated as photocatalyst,[32-34] but this hybrid system has rarely been studied as electrode materials for LIBs.

Based on the aforementioned strategy, we construct MoS_2 nanosheets@TiO_2 nanotubes hybrid nanostructures and used them as electrode materials for the first time. The synthetic process is illustrated in Scheme 1. Firstly, we prefabricate TiO_2@PNT coaxial nanocables based on a sol–gel method, after being calcined in air, the porous TiO_2 nanotubes were obtained. Then the TiO_2 nanotubes are assembled by MoS_2 nanoclusters that consist of ultrathin porous nanosheets after a solvothermal process. The as-prepared MoS_2@TiO_2 were further treated at 800 °C in the atmosphere of 10% H_2 balanced by N_2 to obtain the highly crystalline MoS_2. Finally, the hierarchical and porous MoS_2 nanosheets sustained by porous TiO_2 nanotubes were successfully obtained, which possessed improved cyclic capacity retention and rate capability.

2. Experimental Section

2.1 Material Synthesis

Sulfonated PNTs: Polymeric nanotubes (PNTs) were synthesized by cationic polymerization of divinylbenzene using immiscible initiator nanodroplets of boron trifluoride etherate complex.[35] PNTs (3 g) were added to concentrated sulfuric acid (PNTs : H_2SO_4 = 1: 30, w/w) and the mixtures were ultrasonicated for 10 min to disperse them. After stirring at 40 °C for 24 h, the yellow precipitate was collected by centrifugation and washed thoroughly with ethanol.[36-38]

TiO_2@PNT: 0.1 g of sulfonated PNTs was dispersed in 10 ml of ethanol under sonication for 90 min. The suspension was placed in 0 °C ice bath under high speed magnetic stirring for 20 min. 1.33 g of tetrabutyl titanate (TBT) was rapidly added to the mixture and stirred for 2 h to allow a saturated adsorption of TBT on the surface of sulfonated PNTs. Afterwards, 1 ml of water was introduced into the system and kept stirring at 0 °C for 2 h. The precipitates were separated by centrifugation (4000 rpm) and the product was dried at ambient temperature and subsequently stored in a vacuum oven at 50 °C overnight.[20]

TiO_2 nanotubes: the as-prepared TiO_2@PNT composite was subjected to calcination at 450 °C for 2 h to remove the PNT template and obtain the porous TiO_2 nanotubes. The TiO_2 nanotubes were also calcined at 800 °C in the atmosphere of 10% H_2 balanced by N_2 for 2 h to obtain the rutile TiO_2.

MoS_2@TiO_2: 100 mg of TiO_2 nanotubes were dispersed into glucose solution (30 mL, 0.05 M) by ultrasonication for 5 minutes. And then, 0.3 g sodium molybdate ($Na_2MoO_4 \cdot 2H_2O$) and 0.6 g of thiourea was added. After stirring for 5 minutes, the reaction solution was transferred to a 50 mL Teflon-lined stainless steel autoclave and kept in an electric oven at 200 °C for 24 h. The autoclave was then left to cool down to room temperature in the oven. The black precipitate was collected by centrifugation, washed thoroughly with ethanol, and dried at 80 °C for 12 h. The as-prepared MoS_2 @TiO_2 were further treated at 800 °C in the atmosphere of 10% H_2 balanced by N_2 for 2 h with a heating rate of 1 °C min^{-1} to obtain the highly crystalline MoS_2 nanosheets.

The preparation process of MoS_2 flakes is similar to the one for MoS_2 @TiO_2, except the addition of TiO_2 nanotubes and glucose.

2.2 Characterization

The product morphology was examined using field-emission scanning electron microscopy (FESEM; HITACHI, su-8010) and transmission electron microscopy (TEM; JEOL, JEM-2100). Crystallographic information of the samples was collected using powder X-ray diffraction (XRD; SHIMADZU, Lab X XRD-6000). The specific surface area and pore size distribution of the products were measured using a Brunauer–Emmett–Teller analyzer (BET; ASAP 2020M) at 77 K.

2.3 Electrochemical measurements

The electrochemical tests were performed under ambient temperature using two-electrode coin cells (CR 2016) with lithium serving as both the counter electrode and the reference electrode. The working electrode consisted of an active material (MoS_2@TiO_2), a conductive agent (carbon black, C-NERGY™ Super C65), and a polymer binder (poly(vinylidenedifluoride), PVDF, Aldrich) in a 70: 20: 10 weight ratio. The electrolyte used was 1.0 M $LiPF_6$ in a 50: 50 (w/w) mixture of ethylene carbonate and diethyl carbonate. Cell assembly was carried out in an Ar-filled glovebox with concentrations of moisture and oxygen below 1.0 ppm. Cyclic voltammetry was performed using an electrochemical workstation (CHI 660D). The charge–discharge tests were performed using a NEWARE battery tester.

3. Results and discussion

Fig. 1 shows the morphology of the TiO_2@PNT composite and calcined TiO_2 nanotubes. It can be seen from the scanning electron microscope (SEM) image that the TiO_2 layers are successfully and uniformly coated on the PNTs surface, leading to the formation of TiO_2@PNT nanotubes (Fig. 1A). Transmission electron microscopy (TEM) image indicates the TiO_2 layer is around 85 nm (Fig. 1B). This may be attributed to hydrophilic layer with sulfonic acid groups produced by the sulfonation process, which can induce a favorable adsorption of the tetrabutyl titanate. After calcining the TiO_2@PNT composite in air at 450 °C in air for 2 h, the PNT templates were totally removed and the TiO_2 nanotubes were obtained, as shown in Fig. 1C. It is very clear from the TEM image (Fig. 1D) that the thickness of the TiO_2 shell decreases to approximately 80 nm, due to the slight shrinkage during annealing. In addition, it can be observed that the shell of the nanotubes is mesoporous.

Fig. 2A-D shows the SEM and TEM images of the MoS_2@TiO_2 composite after a solvothermal process and treated at 800 °C in the atmosphere of 10% H_2 balanced by N_2. It reveals that almost every TiO_2 nanotube is uniformly covered with MoS_2 nanosheets, which can be attributed to the assist function of glucose and thiourea (Fig. 2A).[39] A hierarchical structure of the MoS_2@TiO_2 composite's surface can be clearly revealed from the TEM image and the height of the MoS_2 nanosheets is around 120 nm (Fig. 2B). Fig. 2C shows the morphology of the MoS_2@TiO_2 composite after calcination at 800 °C for 2 h to obtain the highly crystalline MoS_2 nanosheets and the MoS_2@TiO_2 composite maintains its tubular and sheets-like structures. The TEM image of the calcined MoS_2@TiO_2 composite displays that the TiO_2 nanotube have an extra porous structure, and the MoS_2 nanosheets is approximately 70 nm in height, on account of the slight shrinkage during annealing (Fig. 2D). Moreover, most of the MoS_2 nanosheets are very thin (~5 nm), less than 7 layers (Fig. 2E). From the HRTEM image in Fig 3F, the

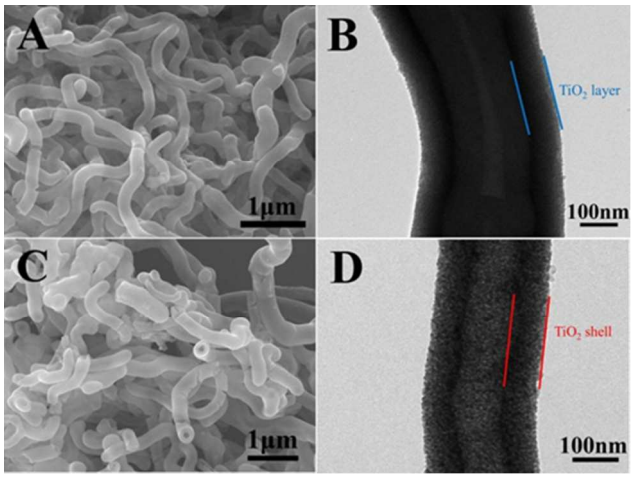

Fig. 1 (A) SEM image and (B) TEM image of TiO_2@PNT nanotubes; (C) SEM image and (D) TEM image of TiO_2 nanotubes after being calcined in air.

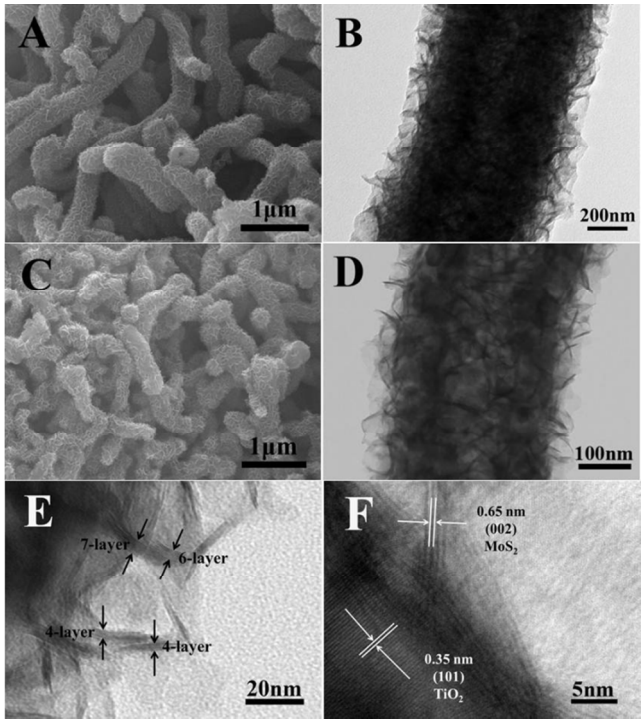

Fig. 2 (A) SEM image and (B) TEM image of MoS_2@TiO_2 composite after a solvothermal process; (C) SEM image and (D) TEM image of MoS_2@TiO_2 composite treated at 800 °C. HRTEM images of several MoS_2 nanosheets (E) and MoS_2@TiO_2 composite (F).

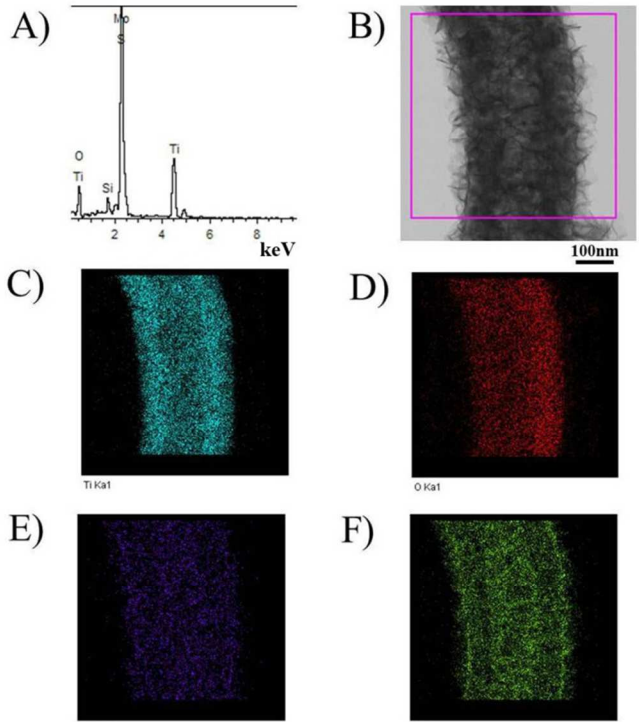

Fig. 3 (A) EDS spectrum of the MoS_2@TiO_2 composite (B) TEM image of MoS_2@TiO_2 composite and the corresponding elemental mapping images of (C) oxygen, (D) sulfur, (E) titanium and (F) molybdenum in the selected area (pink rectangle in (B)).

lattice fringes of TiO_2 nanotubes and MoS_2 nanosheets can be clearly observed, suggesting the well-defined crystal structure and heterojunction (Fig. 2F).

The detailed local elemental composition and the core/shell nanostructure of the as-formed MoS_2@TiO_2 composite was further analyzed by energy dispersive X-ray (EDX) spectroscopy and scanning transmission electron microscopy (STEM) with the results shown in Fig. 3. The elemental mapping images show that the Ti and O elements formed the core of the MoS_2@TiO_2 composite, the shell is consist of Mo and S elements, respectively. It gives a direct proof for the uniform surface modification of MoS_2 nanosheets on TiO_2 nanotubes. Furthermore, the atomic ratio of Mo and Ti is about 1: 1.

The chemical composition of different samples was characterized by using X-ray diffraction (XRD; Fig. 4A). It is clear from pattern of curve I, curve II and curve III that pure MoS_2 (JCPDS card no. 37-1492), anatase TiO_2 (JCPDS card no. 21-1272) and rutile TiO_2 (JCPDS card no. 21-1276) were fabricated after a calcination process. All the diffraction peaks of curve I, curve II and curve III can be discovered from curve IV clearly, indicating that the MoS_2@TiO_2 hybrid nanostructures were successfully obtained, and the TiO_2 nanotubes are mixed with rutile and anatase TiO_2. The

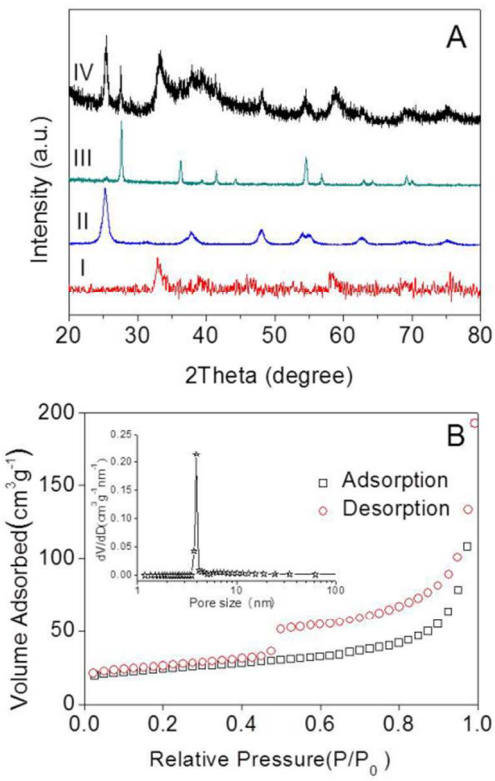

Fig. 4 (A) XRD patterns of MoS_2 flakes (I), TiO_2 nanotubes after being calcined in air at 450 °C (II) TiO_2 nanotubes treated at 800 °C (III) and MoS_2@TiO_2 composite (IV). (B) N_2 adsorption–desorption isotherms of the MoS_2@TiO_2 composite, the inset shows the pore-size distribution calculated from the desorption branch.

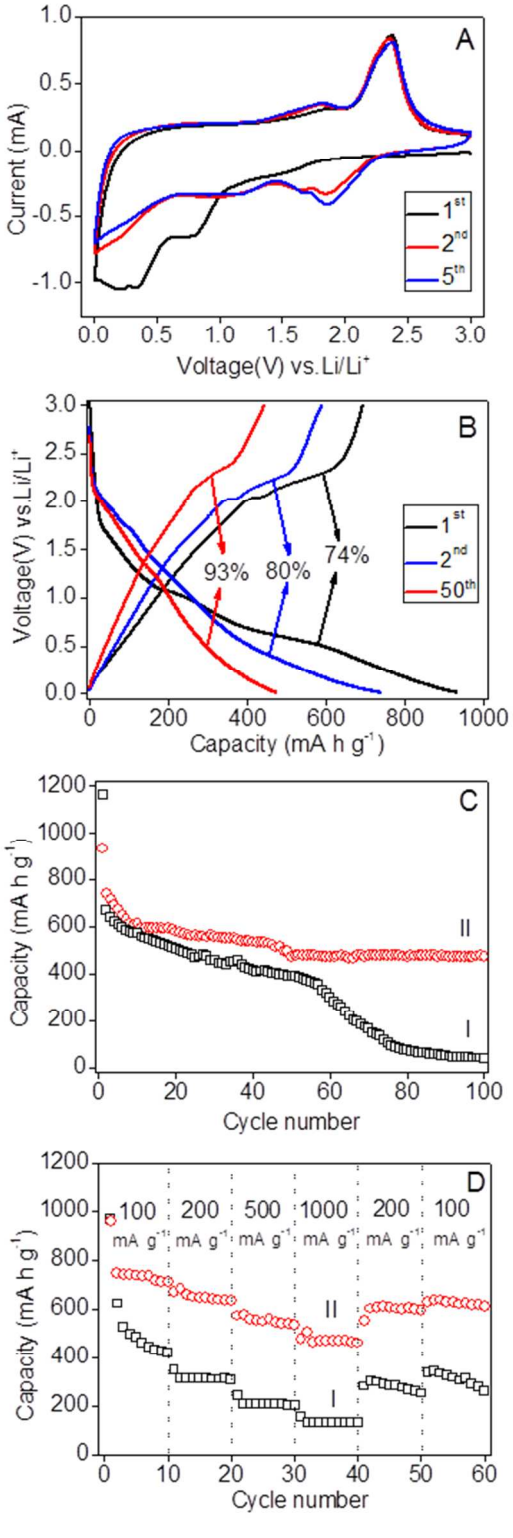

Fig. 5 (A) Representative CVs at a scan rate of 0.5 mV S^{-1} for the first, second, and fifth cycles of MoS_2@TiO_2 hybrid nanostructures. (B) Charge–discharge voltage profiles at a current density of 100 mA g^{-1} of MoS_2@TiO_2 hybrid nanostructures. (C) Comparative cycling performance of MoS_2 flakes (I) and MoS_2@TiO_2 hybrid nanostructures (II) at a current density of 100 mA g^{-1}. (D) Cycling performance of MoS_2 flakes (I) and MoS_2@TiO_2 hybrid nanostructures (II) at different current densities indicated (mA g^{-1}).

nitrogen adsorption/desorption isotherm of the $MoS_2@TiO_2$ composite is shown in Fig. 4B. The Brunauer–Emmett–Teller (BET) specific surface area of $MoS_2@TiO_2$ compsite is 79.8 $m^2 g^{-1}$, and the plot (inset of Fig. 4B) shows that the diameter of most pores is around 4 nm.

The excellent electrochemical performance of the $MoS_2@TiO_2$ hybrid nanostructures as an electrode material for LIBs can be attributed to the following. Fig. 5A shows the cyclic voltammograms (CVs) of $MoS_2@TiO_2$ for the first, second and fifth cycles in the potential window of 0.005-3 V vs. Li^+/Li. As can be seen, the CV behavior is generally consistent with MoS_2 and TiO_2 nanostructures reported previously.[7,10,11,20,21] In the first cathodic sweep, the peak that at 0.7 V is attributed to the intercalation of lithium ions into the MoS_2 lattice which transforms the triangular prism (coordination of Mo by six S atoms) into an octahedral prism structure.[11,33] This peak disappears in the second and fifth discharge processes owing to few amorphous MoS_2 is reformed after the first charge process (lithium extraction). The peak appears at 0.2 V is attributed to the complete reduction process:

$$MoS_2 + 4Li \longrightarrow 4Mo + 2Li_2S \quad (1)$$

In the succedent cathodic sweeps, a couple of new peaks appear at 1.8 V and 1.0 V, perhaps suggesting the presence of a multi-step lithium insertion mechanism.[10,11] There is no significant change in the potentials of the oxidation peaks at 2.4 V, corresponding to the lithium extraction process and the transformation of Mo to MoS_2. In addition, in the second and fifth discharge processes, a pair of weak peaks appear at 1.7 V in the cathodic sweep and 1.8V in the anodic sweep can be discovered, which are attributed to the discharge/charge process of TiO_2:

$$TiO_2 + x(Li^+ + e^-) \longleftrightarrow Li_xTiO_2 (0 < x < 1) \quad (2)$$

Besides, several insertion/extraction peaks between ca. 1.9 and 2.5 V indicate that monoclinic TiO_2 (B) were probably existed in this hybrid nanostructures, these complex TiO_2 constituents were also interesting for the lithium storage.[40,41] These results illustrate that the MoS_2 nanosheets in the $MoS_2@TiO_2$ hybrid nanostructures play a major role in the electrochemical performance, and the TiO_2 nanotubes also make a contribution to the charge-discharge capacity. Fig. 5B shows the charge–discharge voltage profiles of the sample for the first, second and fiftieth cycles. As can be seen, two potential plateaus are observed for the composite electrode in the first discharge, which is in agreement with the above CV study, and it shows a discharge capacity of 931 mA h g^{-1}. The subsequently charge process delivers a capacity of 693 mA h g^{-1}, showing a Coulombic efficiency of 74% (Fig. 5B), which should be mainly due to the gel-like polymeric layer formation on the $MoS_2@TiO_2$ hybrid nanostructures. The charge and discharge capacities in the second cycle are 590 and 737 mA h g^{-1}, respectively, giving a higher Coulombic efficiency of 80%. This value can be retained as 93% even after 50 charge–discharge cycles. The cycling performance of these $MoS_2@TiO_2$ hybrid nanostructures (curve I) is shown in Fig. 5C, and MoS_2 flakes (curve II) fabricated by a similar method are used as comparison.[11] As can be seen, in the case of the $MoS_2@TiO_2$ electrode, the initial discharge step delivers relatively lower capacity of 931 mA h g^{-1}. This is mainly on account of the influence by the TiO_2 nanotubes. However, in the subsequent cycles, the $MoS_2@TiO_2$ hybrid nanostructures possess more stable cycle stability and higher discharge capacities obviously than the MoS_2 flakes. When the cycle number reached about 60th, the MoS_2 flakes reveal a fast fading in capacity. Oppositely, the capacity of the $MoS_2@TiO_2$ hybrid nanostructures becomes extremely stable even at the end of the 100th cycle, which display a value of 472 mA h g^{-1}. The theoretical capacity of the $MoS_2@TiO_2$ hybrid nanostructures can be calculated as follows:

$$C_{MoS_2@TiO_2} = C_{MoS_2} \times mass\%_{MoS_2} + C_{TiO_2} \times mass\%_{TiO_2} \quad (3)$$

on account of the theoretical capacity of the TiO_2 (335 mA h g^{-1}) and MoS_2 (670 mA h g^{-1}), the result is 578 mA h g^{-1}. The above results show that the $MoS_2@TiO_2$ hybrid nanostructures can deliver a stable capacity equal to 80% of their theoretical value even after 100 cycles. It is worthy to be mentioned that the average discharge capacity of our $MoS_2@TiO_2$ hybrid nanostructures is preferable compared to previously reported hierarchical MoS_2 products,[42] a part of hybrid nanostructures such as the $SnO_2@TiO_2$ double-shell nanotubes,[25] TiO_2 supported SnO_2 nanocomposites,[43] $TiO_2@\alpha\text{-}Fe_2O_3$ core/shell arrays[31] and core-sheath $TiO_2@MoO_xS_y$ nanocomposite.[44] Furthermore, the capacity of up-to-date TiO_2 electrode materials is much less than our hybrid nanostructures.[45-47] Fig. 5D displays the comparative cycling performance of $MoS_2@TiO_2$ hybrid nanostructures (curve I) and MoS_2 flakes (curve II) at various current densities. At current densities of 100, 200, 500 and 1000 mA g^{-1}, the capacities of $MoS_2@TiO_2$ hybrid nanostructures are 713, 636, 533 and 461 mA h g^{-1}, respectively. As a comparison, the MoS_2 flakes only reveal poor capacities as follows: 420, 309, 203 and 129 mA h g^{-1}. When the current density returns to 100 mA g^{-1}, the $MoS_2@TiO_2$ hybrid nanostructures still deliver a capacity of 611 mA h g^{-1}. Comparably, an inferior reversible capacity of 262 mA h g^{-1} can be retained by the MoS_2 flakes after 60 cycles. It is thus evident that the $MoS_2@TiO_2$ hybrid nanostructures exhibit much improved cyclic capacity retention and rate capability. The reasons for the enhanced lithium storage properties of the $MoS_2@TiO_2$ hybrid nanostructures could be explained in detail as follows: i) the TiO_2 nanotubes can be regarded as the skeleton of the hybrid nanostructures, thus the electrode materials' large volume change accompanying the process of Li^+ ion charge–discharge can be buffered, which brings about stable cycling performance even at high current rate.[24] ii) The one-dimensional TiO_2 nanotubes make the MoS_2 more dispersed, thus the larger specific surface area could be acquired comparing to the bulk-like and particle-like materials. iii) The porous structure of the TiO_2 nanotubes together with the hierarchical MoS_2 can store more lithium ions, buffer the large volume change to some extent, decrease lithium ions' and electrolyte diffusion length simultaneously.

3. Conclusions

In summary, we have prepared a kind of MoS_2@TiO_2 hybrid nanostructures via a facile two-step method. The characterizations demonstrate that the MoS_2 nanosheets are uniformly supported on the TiO_2 nanotubes surface, which then form the MoS_2@TiO_2 hybrid composites. The existence of the TiO_2 skeleton plays an irreplaceable role to enhance the electrochemical performance of the high-capacity MoS_2. In comparison with the MoS_2 flakes, these unique hybrid nanostructures exhibit greatly enhanced lithium storage properties owing to the integrated smart architecture.

Acknowledgements

This research was supported partially by the National Natural Science Foundation of China (No. 51273158, 21303131); Natural Science Basis Research Plan in Shaanxi Province of China (No. 2012JQ6003, 2013KJXX-49); Ph.D. Programs Foundation of Ministry of Education of China (No. 20120201120048); Program for New Century Excellent Talents in University (NCET-13-0449). The authors are grateful to the Fundamental Research Funds for the Central Universities for financial support.

References

1 J. B. Goodenough and Y. Kim, *Chem. Mater.*, 2010, **22**, 587.
2 M. Armand and J. M. Tarascon, *Nature*, 2008, **451**, 652.
3 P. Wu, N. Du, H. Zhang, J. X. Yu, Y. Qi and D. R. Yang, *Nanoscale*, 2011, **3**, 746.
4 P. Meduri, E. Clark, E. Dayalan, G. U. Sumanasekera and M. K. Sunkara, *Energy Environ. Sci.*, 2011, **4**, 1695.
5 P. G. Bruce, B. Scrosati and J. M. Tarascon, *Angew. Chem. Int. Ed.*, 2008, **47**, 2930.
6 X. W. Lou, C. M. Li and L. A. Archer, *Adv. Mater.*, 2009, **21**, 2536.
7 K. Chang and W. Chen, *Chem. Commun.*, 2011, **47**, 4252.
8 P. G. Bruce , B. Scrosati , J. M. Tarascon , *Angew. Chem. Int. Ed.* 2008 ,**47** , 2930.
9 X. W. Lou, Y. Wang, C. L. Yuan, J. Y. Lee and L. A. Archer, *Adv. Mater.*, 2006, **18**, 2325.
10 K. Chang and W. Chen, *ACS Nano*, 2011, **5**, 4720.
11 S. J. Ding, D. Y. Zhang, J. S. Chen and X. W. Lou, *Nanoscale*, 2012, **4**, 95.
12 J. Xiao, D. W. Choi, L. Cosimbescu, P. Koech, J. Liu and J. P. Lemmon, *Chem. Mater.*, 2010, **22**, 4522.
13 X. H. Cao, Y. M. Shi, W. H. Shi, X. H. Rui, Q. Y. Yan, J. Kong and H Zhang, *small*, 2013, **9**, 3433.
14 C. Q. Feng, J. Ma, H. Li, R. Zeng, Z. P. Guo and H. K. Liu, *Mater. Res. Bull.*, 2009, **44**, 1811.
15 H. Li, W. J. Li, L. Ma,W. X. Chen and J. M. Wang, *J. Alloys Compd.*, 2009, **471**, 442.
16 R. Dominko, D. Arcon, A. Mrzel, A. Zorko, P. Cevc, P. Venturini, M. Gaberscek, M. Remskar and D. Mihailovic, *Adv. Mater.*, 2002, **14**, 1531.
17 L. Kavan, M. Kalba, M. Zukalova, I. Exnar,V. Lorenzen, R. Nesper, and M. Graetzel, *Chem. Mater.*, 2004, **16**, 477.
18 H. S. Zhou, D. L. Li, M. Hibino and I. Honma, *Angew. Chem. Int. Ed.*, 2005, **44**, 797.
19 Y. P. Tang, D. Q. Wu, S. Chen, F. Zhang, J. P. Jia and X. L. Feng, *Energy Environ. Sci.*, 2013, **6**, 2447.
20 H. J. Zhou, L. Liu, X. C. Wang, F. X. Liang, S. J. Bao, D. M. Lv, Y. K. Tang and D. Z. Jia, *J. Mater. Chem. A*, 2013, **1**, 8525.
21 S. H. Liu, Z. Y. Wang, C. Yu, H. B. Wu , G. Wang , Q. Dong, J. S. Qiu, A. Eychmüller, and X. W. Lou, *Adv. Mater.*, 2013, **25**, 3462.
22 J. Y. Huang, L. Zhong, C. M. Wang, J. P. Sullivan, W. Xu, L. Q. Zhang, S. X. Mao, N. S. Hudak, X. H. Liu, A. Subramanian, H. Fan, L. Qi, A. Kushima and J. Li, *Science*, 2010, **330**, 1515.
23 X. W. Lou, D. Deng, J. Y. Lee and L. A. Archer, *J. Mater. Chem.*, 2008, **18**, 4397.
24 M. Gu, Y. Li, X. Li, S. Hu, X. Zhang, W. Xu, S. Thevuthasan, D. R. Baer, J. G. Zhang, J. Liu and C. Wang, *ACS Nano*, 2012, **6**, 8439.
25 J. H. Jeun, K. Y. Park, D. H. Kim, W. S. Kim, H. C. Kim, B. S. Lee, H. Kim, W. R. Yu, K. Kang and S. H. Hong, *Nanoscale*, 2013, **5**, 8480.
26 Z. X. Yang, Q. Meng, Z. P. Guo, X. B. Yu, T. L. Guo and R. Zeng, *J. Mater. Chem. A*, 2013, **1**, 10395
27 M. S. Wu and H. W. Chang, *J. Phys. Chem. C*, 2013, **117**, 2590.
28 L. Qiao, X. H. Wang, L. Qiao, X. L. Sun, X. W. Li, Y. X. Zheng and D. Y. He, *Nanoscale*, 2013, **5**, 3037.
29 M. F. Hassan, M. M. Rahman, Z. P. Guo, Z. X. Chen and H. K. Liu, *J. Mater. Chem.*, 2010, **20**, 9707.
30 Q. Q. Xiong, J. P. Tu, X. H. Xia, X. Y. Zhao, C. D. Gua and X. L. Wang, *Nanoscale*, 2013, **5**, 7906.
31 Y. S. Luo, J. S. Luo, J. Jiang, W. W. Zhou, H. P. Yang, X. Y. Qi, H. Y. S. Luo, J. S. Luo, J. Jiang, W. W. Zhou, H. P. Yang, X. Y. Qi, H. *Energy Environ. Sci.*, 2012, **5**, 6559.
32 W. J. Zhou, Z. Y. Yin, Y. P. Du , X. Huang, Z. Y. Zeng, Z. X. Fan, H. Liu, J. Y. Wang and H. Zhang, *small*, 2013, **9**, 140.
33 Q. J. Xiang, J. G. Yu and M. Jaroniec, *J. Am. Chem. Soc.*, 2012, **134**, 6575.
34 W. K. Ho, J. C. Yu, J. Lin, J. G. Yu, and P. S. Li, *Langmuir*, 2004, **20**, 5865.
35 W. Ni, F. Liang, J. Liu, X. Qu, C. Zhang, J. Li, Q. Wang and Z. Yang, *Chem. Commun.*, 2011, **47**, 4727.
36 X. Xu, J. Liang, H. Zhou, D. M. Lv, F. X. Liang, Z. L. Yang, S. J. Ding and D. M. Yu, *J. Mater. Chem. A*, 2013, **1**, 2995–2998.
37 X. Xu, G. R. Yang, J. Liang, S. J. Ding, C. L. Tang, H. H. Yang, W. Yan, G. D. Yang and D. M. Yu, *J. Mater. Chem. A*, 2014, **2**, 116.
38 X. Xu, J. Liang, H. Zhou, S. J. Ding and D. M. Yu, *RSC Adv.*, 2014, **4**, 3181.
39 S. J. Ding, J. S. Chen, and X. W. Lou, *Chem. Eur. J.*, 2011, **17**, 13142.
40 L. Kavan, *Chem. Rec.*, 2012, **12**, 131.
41 B. Laskova, M. Zukalova, A. Zukal, M. Bousa, L. Kavan, *J. Power Sources*, 2014, **246**, 103.
42 P. L. Sun, W. X. Zhang, X. L. Hu, L. X. Yuan, and Y. H. Huang, *J. Mater. Chem. A*, 2013, DOI: 10.1039/C3TA13994H.
43 Y. M. Lin, R. K. Nagarale, K. C. Klavetter, A. Heller and C. B. Mullins, *J. Mater. Chem.*, 2012, **22**, 11134.
44 Y. Qiao, X. L. Hu, Y. Liu, G. Liang, M. C. Croftc and Y. H. Huang, *J. Mater. Chem. A*, 2013, **1**, 15128.
45 J. S. Chen, Y. L. Tan, C. M. Li, Y. L. Cheah, D. Y. Luan, S. Madhavi, F. Y. C. Boey, L. A. Archer and X. W. Lou, *J. Am. Chem. Soc.*, 2010, **132**, 6124.
46 Y. G. Guo, J. S. Hu and L. J. Wan, *Adv. Mater.*, 2008, **20**, 2878.
47 S. H. Liu, H. P. Jia, L. Han, J. L. Wang, P. F. Gao, D. D. Xu, J. Yang, and S. N. Che, *Adv. Mater.*, 2012, **24**, 3201.